

Materials and Methods

Cell lines and plasmids

A U2OS cell line stably expressing GFP-CENP-A and mCherry- α -tubulin was generated as described (1). U2OS cell lines stably expressing H2B-GFP with and without mCherry- α -tubulin (kind gift from S. Geley, Innsbruck Medical University, Austria) were generated as previously described (28). The HeLa BAC line stably expressing CENP-E-GFP (www.mitocheck.org) has been described previously (20). All cell lines were grown in Dulbecco's Modified Eagle Medium (DMEM) supplemented with 10% foetal bovine serum (FBS; Invitrogen) at 37 °C with 5% CO₂. To express fluorescently labelled proteins, cells were transfected for 36h using either X-tremeGENE (Roche) or Lipofectamine 2000 (Invitrogen) with 2 μ g of the following constructs: TTL-YFP (29), Ran-T24N-mCherry (5) (gift from I. Cheeseman, Whitehead Institute, USA), GFP-SIRT2 (gift from E. Verdin, University of California, San Francisco, USA) and mCherry- α -tubulin.

RNAi and immuno blot analysis

To perform RNA interference (RNAi)-mediated protein depletion, cells were transfected at 30–50% confluence using Lipofectamine RNAiMAX (Invitrogen) with 50 nM siRNAs between 48–72 h. The following siRNAs were used: TTL#1 5'-CAGCCACCAAUCAGUAACU-3', TTL#2 5'-CCCUGAAUCUUAUGUGAUU-3', TTL#3 5'-GUGCACGUGAUCCAGAAAU-3', α -TAT1 5'-AACCGCCAUGUUGUUUAUAUU-3' (ref. (30)). Protein levels were monitored by immuno blot using the following antibodies: rabbit anti-detyrosinated α -tubulin (AB3201, Merck Millipore), diluted 1:2000; rat anti-tyrosinated α -tubulin (YL1/2) (MCA77G, AbD Serotec), diluted 1:10000; mouse anti- α -tubulin (clone B512, Sigma), diluted 1:10000; rabbit anti-TTL (13618-1-AP, Proteintech), diluted 1:2000; mouse anti-acetylated α -tubulin (clone 6-11B-1, Sigma), diluted 1:1000; mouse anti-glutamylated tubulin (GT335, AG-20B-0020, Adipogen), diluted 1:2000; rabbit anti-polyglutamylation (polyE; AG-25B-0030, Adipogen), diluted 1:2000; mouse anti-GAPDH (60004-1-Ig, Proteintech), diluted 1:25000. HRP-conjugated secondary antibodies (Jackson ImmunoResearch), diluted 1:10000, were visualized using the ECL system (Bio-Rad).

Drug treatments

To inhibit CENP-E, 20 nM GSK-923295 (MedChemexpress) was added to the cell culture media just before live cell imaging. To inhibit TCP, 15–20 μ M parthenolide (Sigma) was added to the cells just before or during live cell imaging, or 3–4h prior to fixation. To inhibit SIRT2, 30 μ M AGK2 (Sigma) was added to the cells 4h prior to fixation. To induce monopolar spindles by inhibition of Eg5 (kinesin-5), 5 μ M S-Trytil-L-Cysteine (STLC; Sigma) was added to the cell culture media 2 h before fixation.

Immunofluorescence microscopy

U2OS cells were grown on glass coverslips and fixed by ice-cold methanol for 4 min at -20 °C. The following primary antibodies were used: rabbit anti-detyrosinated α -tubulin (AB3201, Merck Millipore), diluted 1:200; mouse anti- α -tubulin (clone B512, Sigma), diluted 1:2000; human anti-centromere antibodies (ACA) (90C-CS1058-1 ML, Fitzgerald), diluted 1:4000; mouse anti-acetylated α -tubulin (clone 6-11B-1, Sigma), diluted 1:200; rabbit anti-centrin (kind gift of Iain Cheeseman, Whitehead Institute for Biomedical Research, Cambridge, MA, USA), diluted 1:2000. Alexa Fluor 488, 568, and 647 (Invitrogen) were used as secondary antibodies (diluted 1:1000). DNA was counterstained with DAPI (1 μ g/ml; Sigma-Aldrich). Images were acquired in an AxioImager Z1 (100 \times Plan-Apochromatic oil differential interference contrast objective lens, 1.46 NA) equipped with a CCD camera (ORCA-R2, Hamamatsu) operated by Zen software (Zeiss). Blind deconvolution of images was performed using Autoquant X software (Media Cybernetics). Images were processed in Photoshop CS4 (Adobe) and represent maximum intensity projections of a deconvolved stack. Co-localization analysis of CENP-E and detyrosinated tubulin was performed using the co-localization plugin package in ImageJ (31). Kinetochore-to-pole distances were measured using a custom program written in MATLAB 8.1 (The Mathworks), which determines the 3D-distance between the centroid of a kinetochore and the microtubule minus-ends at the spindle pole or the middle point between centrioles.

Live cell imaging

U2OS-H2B-GFP, U2OS-H2B-GFP/mCherry- α -tubulin cells and U2OS-GFP-CENP-A/mCherry- α -tubulin cells were cultured in 35 mm glass-bottomed dishes (14 mm, No. 1.5, MatTek Corporation). Cell culture media was changed to L15 (Invitrogen) prior to imaging. Time-lapse imaging was performed in a heated chamber (37 °C) using a 100x 1.4 NA Plan-Apochromatic differential interference contrast objective mounted on an inverted microscope (TE2000U; Nikon) equipped with a CSU-X1 spinning-disk confocal head (Yokogawa Corporation of America) and with two laser lines (488 nm and 561 nm). Images were detected with an iXonEM+ EM-CCD camera (Andor Technology). Eleven 1 μ m-separated z-planes covering the entire volume of the mitotic spindle were collected every 2 min. Image processing was performed in ImageJ (31). All displayed images represent maximum-intensity projections of z-stacks.

Protein purification

Human tubulin was purified from HeLa S3 cells (ATCC® CCL-2.2™). Cells were grown for 1 week in 4 spinner bottles then spun down and resuspended in 1 vol (app. 10 ml) of the lysis buffer BRB80 (80 mM K-Pipes pH 6.8, 1 mM EGTA, 1 mM MgCl₂), containing 1 mM β -mercaptoethanol, 1 mM PMSF and other protease inhibitors. The cells were broken using the French press at 4°C. The lysate was further incubated on ice with

occasional pipetting to depolymerize all microtubules, and then spun down 30 min at 145,000 g at 4°C. The supernatant was spun down again as above. The supernatant was supplemented with 30% final glycerol and 1 mM GTP and incubated for 30 min in a 30°C water bath. The polymerized microtubules were then pelleted (30 min at 185,000g and 30°C). Microtubules were depolymerized on ice in a minimal volume (0.5–1 ml) of BRB80/0.3 M KCl by pipetting up and down occasionally for 30 min. Soluble tubulin was then recovered after a 20 min spin (20 min, 4°C). Tubulin sample was then split in two and incubated for 5 min at 30°C, either without carboxypeptidase A (CPA, Sigma, C9268, app. 6 U/mg of tubulin) to obtain tyrosinated (T) tubulin or with CPA to obtain detyrosinated (D) tubulin. Tubulins were then incubated for 20 min with 0.6 ml of DEAE resin. The resin was packed onto a Econo-Column, washed 3x with 1 vol of BRB80/0.3 M KCl and tubulins were eluted in small fractions (100-200 µl) with BRB80/0.5 M KCl. Bradford positive fractions were concentrated on a Vivaspin ultrafiltration spin column (Sartorius Stedim Biotech, Germany), snap frozen and stored at -80°C. Alternatively, the Bradford-positive fractions were concentrated by polymerization in presence of GTP and glycerol for 30 min at 30°C, pelleting and depolymerization in BRB80. Single molecule assays using microtubules with the same post-translational modification but prepared using these different concentration steps produced highly similar results, so these data were pulled together. Porcine and bovine tubulin was purified from cow or pig brains by thermal cycling and chromatography and then labelled with HiLyte647 as in ref. (32). CENP-E kinesin from *Xenopus laevis* with C-terminal GFP fusion (CE473-GFP) was purified using protocol in ref. (33) with modifications. Protein expression was induced at 16°C for 19 h with 50 µM IPTG, cells were lysed on ice for 60 min in lysis buffer containing 2.7 mM KCl, 288 mM NaCl, 1.5 mM KH₂PO₄, 8 mM Na₂HPO₄ (pH 8), 50 mM imidazole, 5 mM MgCl₂, 0.5 mM EGTA, 0.1 mM ATP, 10 mM β-mercaptoethanol, 0.1% Igepal, 1 mg/ml lysozyme, 1 µl/ml benzonase and Complete EDTA-free protease inhibitors (Roche). After incubation with Ni-NTA, protein was eluted with 300 mM Imidazole in lysis buffer. CENP-E containing fractions were diluted 10 times with SP buffer (15 mM Hepes, pH 6.8, 2 mM MgCl₂, 0.5 mM EGTA, 1 mM DTT, 0.1 mM ATP), loaded onto SP Sepharose Fast Flow (GE Healthcare) column, washed with SP buffer supplemented with 0.1 M KCl. CENP-E was eluted in same buffer but containing 0.5 M KCl. The peak fractions were pooled, supplemented with 25% glycerol, aliquoted, frozen in liquid nitrogen and stored at -80°C.

Single molecule motility assay

Microtubules were polymerized as in ref. (32) using modified HeLa tubulin and bovine HiLyte-labeled tubulin in 10:1 molar ratio. Additional control experiment was carried out to verify that bovine tubulin incorporated in the same low proportion in T- vs. D-MTs by determining the brightness of these microtubules. This was done by using rectangular regions 10 pixel-wide and custom written software in ImageJ, which records the peak intensities along microtubule length minus the intensities along a similar linescan but in the adjacent region without any microtubules. Brightness of T- vs. D-MTs was highly similar (Fig. S8C). CENP-E motility was examined using custom-made flow chambers assembled with plasma cleaned, then silanized coverslips, as in ref. (34). Specimen temperature was

maintained at $32.0 \pm 0.5^\circ\text{C}$. Taxol-stabilized microtubules were attached to coverslip through anti-tubulin antibodies (Serotec) and the surface was blocked with Pluronic-F127. CENP-E at ~ 15 nM was flown continuously at $15 \mu\text{l}/\text{min}$ and imaged in the motility buffer (80 mM Pipes pH 6.9, 4 mM MgCl_2 , 1 mM EGTA, 4 mg/ml BSA, 2 mM DTT, 2 mM MgATP, 7.5–10 μM Taxol, 50 $\mu\text{g}/\text{ml}$ glucose, 68 $\mu\text{g}/\text{ml}$ catalase, 0.1 mg/ml glucose oxidase and 0.5% β -mercaptoethanol). Residual concentration of KCl from CENP-E protein storage buffer was 3.5 mM. Images were acquired using Andor iXon3 (999 EM Gain, 5x Gain, 14-bit readout) and Nikon total internal reflection fluorescence microscopy system described in ref. (23). CENP-E images were captured in GFP channel using 60 ms exposure every 200 ms for 5 min; Hilyte647 microtubules were recorded with 100 ms exposure at the beginning and end of each GFP series. To verify that the same experimental conditions were used for chambers containing T- vs. D-MTs, the bovine rhodamine-labeled microtubules were introduced into the same chambers. CENP-E motility on bovine microtubules from different chambers was highly similar (Fig. S8D), indicating that the difference in CENP-E motility on T- vs. D-MTs was indeed caused by their different lattices. CENP-E-GFP images in Movie S3 were captured using 50 ms exposure every 100 ms.

Analysis of CENP-E motility

Kymographs were created using Metamorph (Molecular Devices). Only clear tracks that did not intersect with other lines were analyzed, unless velocities before and after the crossings were similar. Velocity for each GFP dot was calculated from the slope of the corresponding kymograph. Characteristic run length (r) for each type of microtubules was determined using cumulative probability distribution function (35). Briefly, a cumulative probability distribution of individual run lengths (x) was fitted to an exponential decay function with a shift $x_0 = 0.5 \mu\text{m}$ to account for underestimation of short run lengths: $1 - \exp(-(x-x_0)/r)$ (Fig. S8E). Average residency time for moving motors was 2.7 ± 0.2 and 3.1 ± 0.1 s for T- and D-MTs, respectively; this is significantly shorter than the characteristic bleaching time 49.8 ± 2.3 s, so the runs terminated due to CENP-E-GFP dissociation. We only included the microtubule tracks longer than $4.8 \mu\text{m}$, which ensured that $> 80\%$ of CENP-E runs terminated before the molecules reached the microtubule ends. Furthermore, the mean lengths of microtubules polymerized from different tubulins were similar (Fig. S8F), ensuring that the run lengths were measured under similar conditions. Brightness of the moving dots was quantified by selecting circular regions around the GFP dots (7 pixels in diameter) on the first 3 frames after the start of imaging; background signal was quantified using nearby regions and then subtracted. Uneven laser illumination was accounted for as in ref. (34). Brighter CENP-E-GFP dots tended to move slower, so only the dimmer dots (highlighted area in Fig. S8G) were selected for velocity and run length quantifications.

Description of laser trap and other devices

Our instrument is an improved version of the system described in ref. (36). Briefly, upright Zeiss AxioImager.Z2 microscope was modified to accommodate 3 lasers and to improve its mechanical stability, as illustrated by power spectrum of a trapped bead (Fig. S12A). Sample scanning is done with ASI stage (PZU-4004), controlled electronically or with a joystick. Mounted on this stage is a three-axis piezo-electric stage (Physik Instrumente P-561.3DD), which controls the specimen's position in increments of 1 nm over a 45 x 45 x 15 μm volume. An acousto-optical deflector (AOD, IntraAction Corp., DTD-274HA6 2-AXIS DEFLECTOR) is used for steering the trapping laser beam (IPG Photonics, YLR-10-1064-LP, 1064 nm) in the x,y plane perpendicular to the microscope axis z . Conversion parameters for the AOD input frequency are obtained using video tracking of a trapped bead in x,y with Metamorph (Fig. S12B). Electronically controlled actuator (Standa) adjusts focus of the trapping beam, thereby moving a trapped bead along the z axis (conversion coefficient is 223 nm of laser focus motion per 1 mm displacement of focusing lenses). A vertically polarized laser beam (780 nm, Qioptiq iFlexx 2000) is imaged with a quadrant photodetector (QPD, custom built). Signals from the four elements of QPD are preamplified and passed through a differential amplifier (frequency range 0-100 kHz). This supplies normalized x - and y - signals and a third signal, which is called "sum" of intensities from all four QPD quadrants, subsequently digitized by a 16-bit A/D board FPGA (National Instruments, PCIe-7842R). Alignment of QPD and laser beams was verified with 3-dimensional calibration, during which a bead was moved in x,y,z with the piezo-electric stage (Fig. S12C); the crosstalk between different signals was <5%. In all our experiments the QPD was sampled at 50 kHz and the data were converted to 5 kHz by 10 points averaging. The QPD and trap stiffness were calibrated for each CENP-E-coated bead immediately prior to the experimental measurements (see below). Programs for calibration and instrument control were written in LabVIEW 6i (National Instruments). All experiments used 1.3-NA Plan-Neofluar 100X objective (Zeiss Inc.). A 488 nm laser (Coherent, Sapphire 488-20/460-CDRH laser) was used for fluorescence excitation of GFP on CENP-E-GFP-coated beads. Cascade-650 CCD camera (Photometrics) recorded the fluorescent and differential interference contrast (DIC) images of the beads and microtubules.

Bead preparation and assay conditions for laser trapping experiments

Streptavidin polystyrene beads 0.54 μm in diameter (Spherotech) were incubated for 1.5 h with biotinylated anti-6X-His tag antibodies (Abcam) in PBS (140 mM NaCl, 2.7 mM KCl, 10.1 mM Na_2HPO_4 , 1.8 mM KH_2PO_4 , pH 7.2) supplemented with 7.3 mg/ml BSA and 1.8 mM DTT. Beads were washed extensively and stored in BRB80 supplemented with 3 mM MgCl_2 , 6.9 mg/ml BSA, 0.9 mM DTT and 5 mg/ml casein at 4°C for not more than 2 weeks. Prior to each experiment the beads were washed, resuspended in BRB80 with 0.15 mM MgATP , 2mM DTT, 4 mg/ml BSA, and incubated for 1.5 h with 9 nM CENP-E protein, precentrifuged to remove aggregates. Beads were washed twice and used immediately in two experimental flow chambers, one with T-MTs and the other with D-MTs. Assay conditions were as in single molecule assay except microtubules were spiked

with rhodamine-labeled bovine tubulin and the motility buffer was supplemented with 0.5 mg/ml casein. Data reported were obtained with 9 bead preparations, the fraction of moving beads was similar for T-MTs (28%) and D-MTs (23%), based on measurements from 118 and 136 beads, respectively.

QPD and stiffness calibrations

Bead coated with CENP-E was held in the laser beam approximately 1 μm below the coverslip. Position of the tracking beam was adjusted to achieve zero QPD voltage response, thereby ensuring that the trapped bead is positioned at the center of the tracking beam. With AOD the bead was moved in 10 nm steps from $-0.5 \mu\text{m}$ to $0.5 \mu\text{m}$ along the x - and y -axes. The obtained QPD voltage response was fitted with a 7th order polynomial (Fig. S12D), and the fitting coefficients were used to obtain bead's displacement during the experiment. The stiffness of the laser trap for the same bead was then determined based on equipartition theorem (37). The stiffness ranged from 0.054 to 0.075 pN/nm, with average 0.064 ± 0.001 and 0.066 ± 0.001 pN/nm for x - and y -axes, respectively.

Force measurements

After calibrations, the bead was positioned near a taxol-stabilized coverlip-attached microtubule using the joystick-controlled ASI stage and the more accurate adjustment of the x , y position was achieved with the piezo stage. Actuator was then used to adjust focus of the trapping beam to bring the bead closer to the coverslip attached microtubule. Bead was kept in this position for 30 s to promote microtubule binding. Microtubules that were aligned along y axis were chosen for this work; the maximum deviation was < 3 deg, introducing $< 1\%$ error in the measurement along this axis. The displacement of the bead due to CENP-E activity was recorded with QPD. DIC images of some beads were also recorded continuously with 10 ms exposure using a CCD camera to confirm that the bead tracking from image sequences was consistent with the QPD recordings (Fig. S9A). Images of rhodamine-labeled microtubules and GFP-signal from the CENP-E coated trapped beads were recorded after each measurement. To avoid laser damage to CENP-E protein, each measurement did not exceed 120 s. Data reported in main figures are based on 12 beads for each type of microtubules, generating the total number of force spike events 604 and 394, for T- and D-MTs, respectively.

Analysis of force distribution and bead binding time

Bead displacement was converted to force using trap stiffness for each bead. The corresponding distribution had a prominent peak at zero force, when the microtubule-free bead was positioned at the center of the optical trap (Fig. S9B). This peak was fitted to a Gaussian function up to 1 pN force, and using these parameters a Gaussian distribution was extended for the entire force range. The simulated curve was subtracted from the original

“raw” force distribution to obtain “final” signal (Fig. S9B). This procedure was repeated for each bead, the obtained distributions were summed up and normalized to the total number of data points ($n = 1.7 \times 10^6$ and 1.4×10^6 for T- and D-MTs, respectively) (Fig S9C). To obtain bead binding time, the force traces were filtered by 100 point averaging and 2 pN cut off was used to reduce contribution from noise. For each binding event, the time that the bead was bound to microtubule from the 2 pN force and until the detachment was determined using MATLAB; the minimal included binding time was 20 ms (Fig. S9D).

Analysis of CENP-E stepping and detachment

Force tracings were averaged to 0.5 kHz, steps were identified using the algorithm from ref. (38), and the size of these steps and their duration (dwell times) were determined. Average CENP-E step size in each microtubule direction was determined by fitting a Gaussian curve to the respective histogram distribution of all steps (Fig 2E) or in the 2 pN force bins (Fig. S9E). The total number of forward steps for T- and D-MTs was 5146 and 3427, respectively. The total number of backward steps for T- and D-MTs was 1731 and 1114, respectively. Stepping probability with different force was determined as in ref. (39) by counting the number of forward and backward steps within 1 pN bins. Bead detachment was defined as a backward step greater than 30 nm. The total number of detachment events for T- and D-MTs was 491 and 269, respectively. The detachment rate was obtained by dividing the number of detachments in 1 pN bin by the total time the beads spent within that bin (Fig. S9H).

Theoretical description of CENP-E stepping

Energetics and force dependency of CENP-E stepping were analyzed as in ref. (39). Briefly, stochasticity and directionality of CENP-E stepping were represented with two energy barriers ΔG^+ and ΔG^- , corresponding to the forward and backward transitions (40) (Fig. S9I). In presence of external opposing force F , the energy potentials for forward and backward stepping become $\Delta G^+ + Fd$ and $\Delta G^- - Fd$, respectively, where d is the characteristic distance against the load. According to the Boltzmann energy distribution, the probabilities for steps in the forward p_{frw} and backward p_{bkw} directions are given by:

$$p_{frw} \sim e^{-\frac{\Delta G^+ + Fd}{k_B T}}, \quad p_{bkw} \sim e^{-\frac{\Delta G^- - Fd}{k_B T}}, \quad p_{frw} + p_{bkw} = 1 \quad (1)$$

Following functions for p_{frw} and p_{bkw} satisfy the system (1):

$$p_{frw} = \frac{e^{-\frac{\Delta G^+ + Fd}{k_B T}}}{e^{-\frac{\Delta G^+ + Fd}{k_B T}} + e^{-\frac{\Delta G^- - Fd}{k_B T}}}, \quad p_{bkw} = \frac{e^{-\frac{\Delta G^- - Fd}{k_B T}}}{e^{-\frac{\Delta G^+ + Fd}{k_B T}} + e^{-\frac{\Delta G^- - Fd}{k_B T}}} \quad (2)$$

By dividing the numerator and denominator in functions (2) by $e^{-\frac{\Delta G^-}{k_B T}}$, the expressions for p_{frw} and p_{bkw} can be rewritten:

$$p_{frw} = \frac{Ae^{-\frac{Fd}{k_B T}}}{e^{\frac{Fd}{k_B T}} + Ae^{-\frac{Fd}{k_B T}}}, \quad p_{bkw} = \frac{e^{\frac{Fd}{k_B T}}}{e^{\frac{Fd}{k_B T}} + Ae^{-\frac{Fd}{k_B T}}} \quad (3)$$

where $A = e^{\frac{\Delta G^- - \Delta G^+}{k_B T}}$. Functions (3) with parameters A and d were used to fit the experimentally determined stepping probability as a function of force.

The ratio of the forward and backward stepping probabilities is given by:

$$p_{frw} / p_{bkw} = Ae^{-\frac{2Fd}{k_B T}} \quad (4)$$

Results of applying these equations to the experimental data are presented in Table S1.

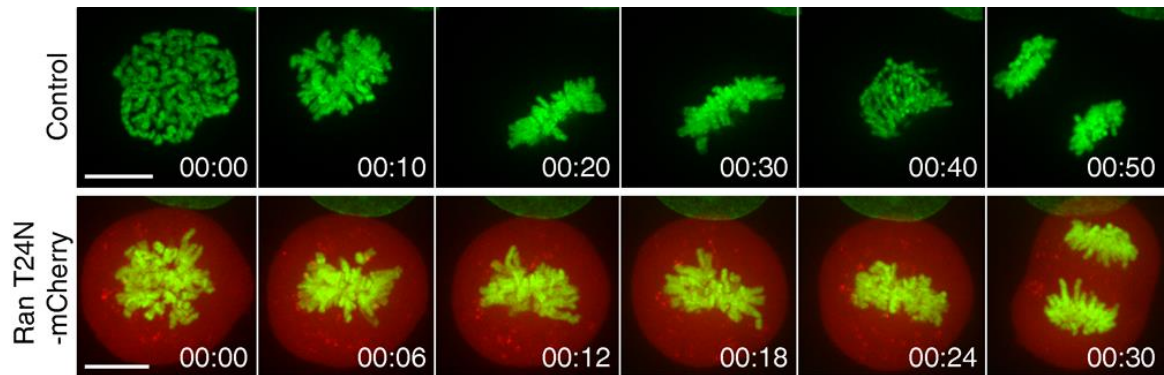


Fig. S1 – Chromosomes successfully congress in cells expressing RanT24N dominant negative mutant. Spinning disk confocal live cell imaging of U2OS cells stably expressing H2B-GFP. Cells were transiently transfected with RanT24N-mCherry, a dominant negative mutant of Ran which binds RCC1 and inhibits its nucleotide exchange. Recording was performed 48h after transfection. Cells completed mitosis in 36 ± 12 min (mean \pm SD). N= 5 cells from 2 independent experiments. Scale bar=10 μ m. Time = h:min.

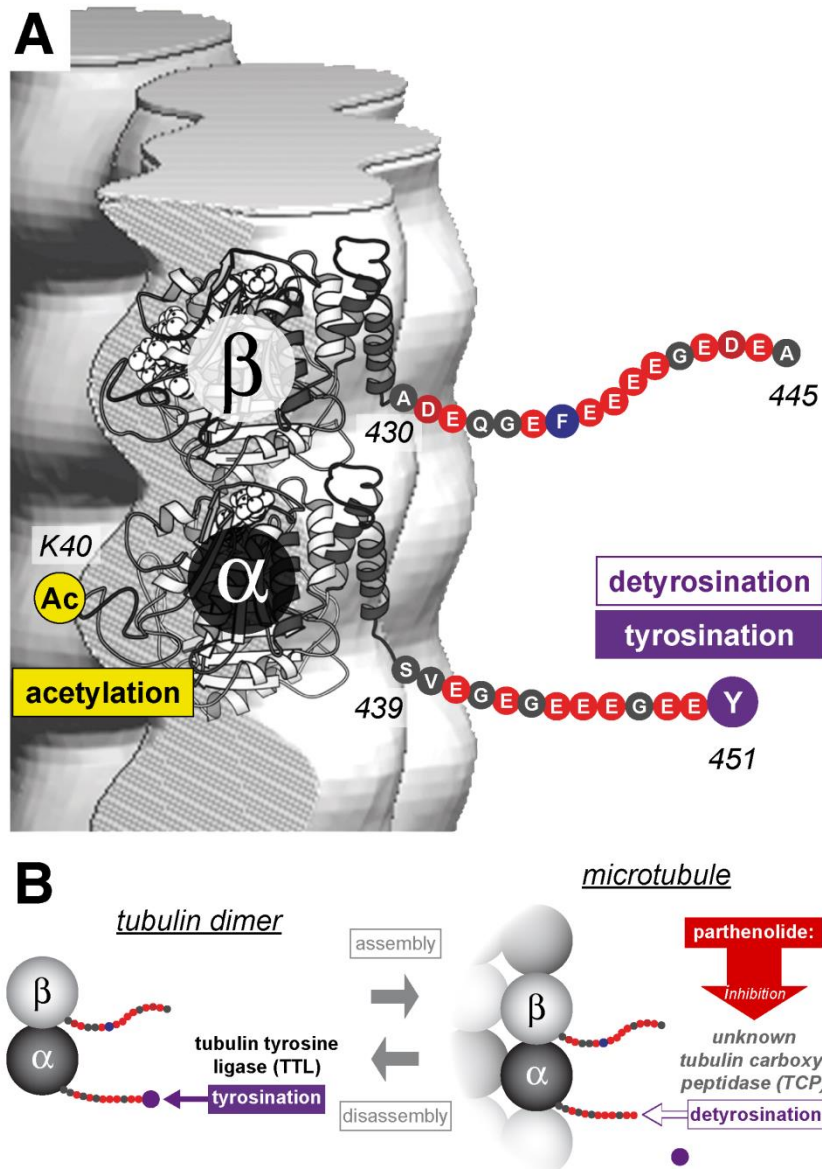


Fig. S2 – The detyrosination/tyrosination cycle. (A) Schematic representation of microtubule lattice, featuring one tubulin dimer and its C-terminal tails. The detyrosination/tyrosination cycle takes place at the C-terminal of α -tubulin. Acetylation of α -tubulin takes place on lysine 40 residue that faces inside the microtubule lumen. Modified from ref. (10). (B) Schematic representation of the detyrosination/tyrosination cycle. Tubulin tyrosine ligase (TTL) acts on soluble tubulin, whereas detyrosination takes place on polymerized tubulin via the activity of a yet unidentified tubulin carboxypeptidase (TCP), which is inhibited by parthenolide.

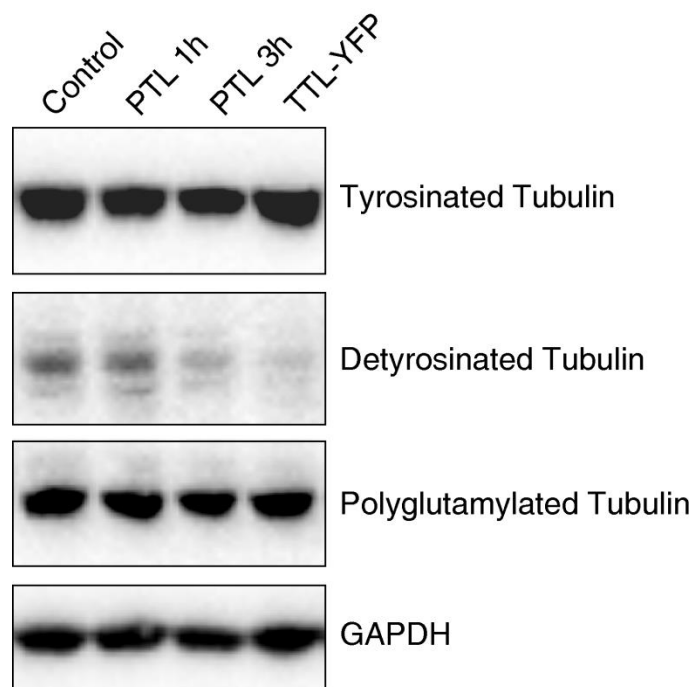


Fig. S3 – TTL overexpression and TCP inhibition with parthenolide specifically affects the tubulin (de)tyrosination state. Microtubule tyrosination, detyrosination and polyglutamylation were examined by immunoblotting with antibodies against tyrosinated, detyrosinated and polyglutamylated (polyE) tubulin, respectively. Protein lysates of U2OS cells were obtained 1h and 3h after adding 20 μ M parthenolide (PTL) and 24h after TTL-YFP transfection. GAPDH was used as loading control. Please note that the polyE antibody is highly sensitive to even minute amounts of polyglutamylation.

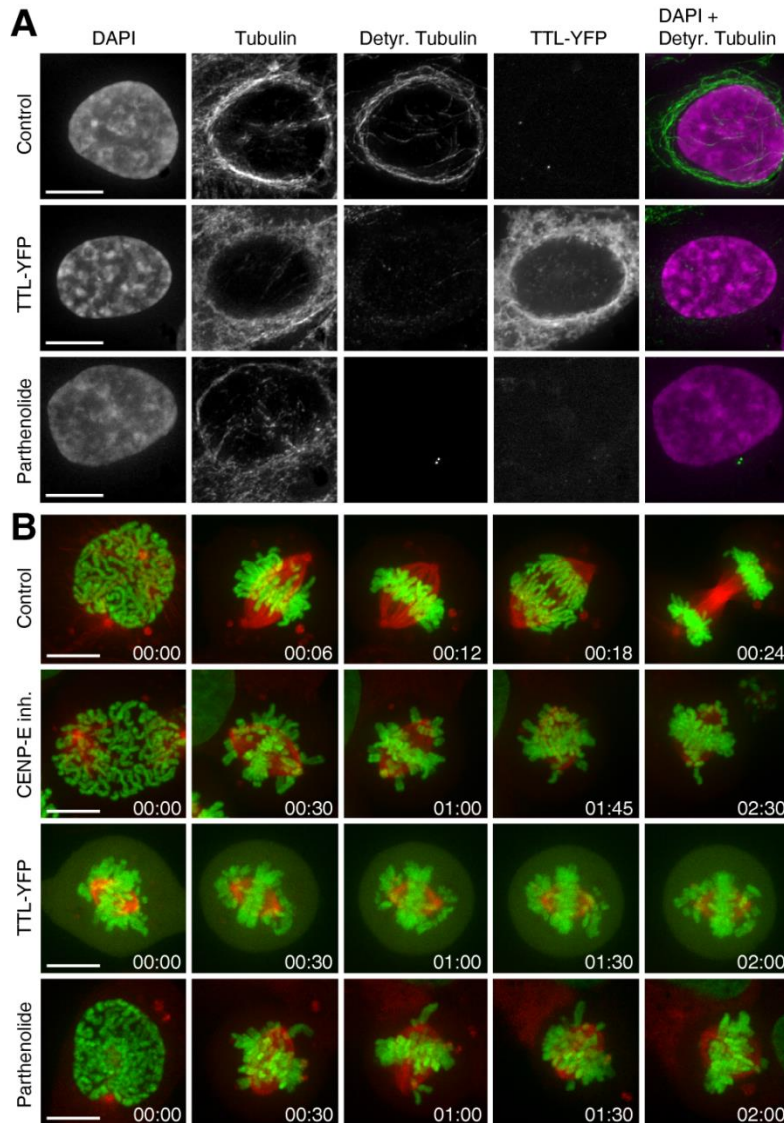


Fig. S4 – TTL overexpression or TCP inhibition prevent microtubule detyrosination.

(A) Deconvolved wide-field immunofluorescence images of methanol-fixed U2OS cells stained for DNA (DAPI), α -tubulin and detyrosinated tubulin. TTL-YFP signal was detected by direct fluorescence. Detyrosination of spindle microtubules was undetectable after TTL-YFP over-expression or treatment with parthenolide. Scale bar=10 μ m. (B) Spinning-disk confocal live cell imaging of U2OS cells stably expressing H2B-GFP and mCherry tubulin. CENP-E motor activity was inhibited by GSK923295, while microtubule detyrosination was prevented either by transient transfection of TTL-YFP or by the TCP inhibitor parthenolide. Chromosome congression was severely impaired in 100% of the cells over-expressing TTL-YFP (6 cells, 3 independent experiments), and in 100% cells treated with Parthenolide (24 cells, 2 independent experiments). These defects were indistinguishable in both treatments and prevailed for the duration of our recordings (at least 2h). In most cases, we noticed that mitotic spindles got shorter over time after 2h parthenolide treatment and cells eventually died. This possibly reflects some side-effects of the drug when compared with TTL overexpression. Scale bar=10 μ m. Time = h:min.

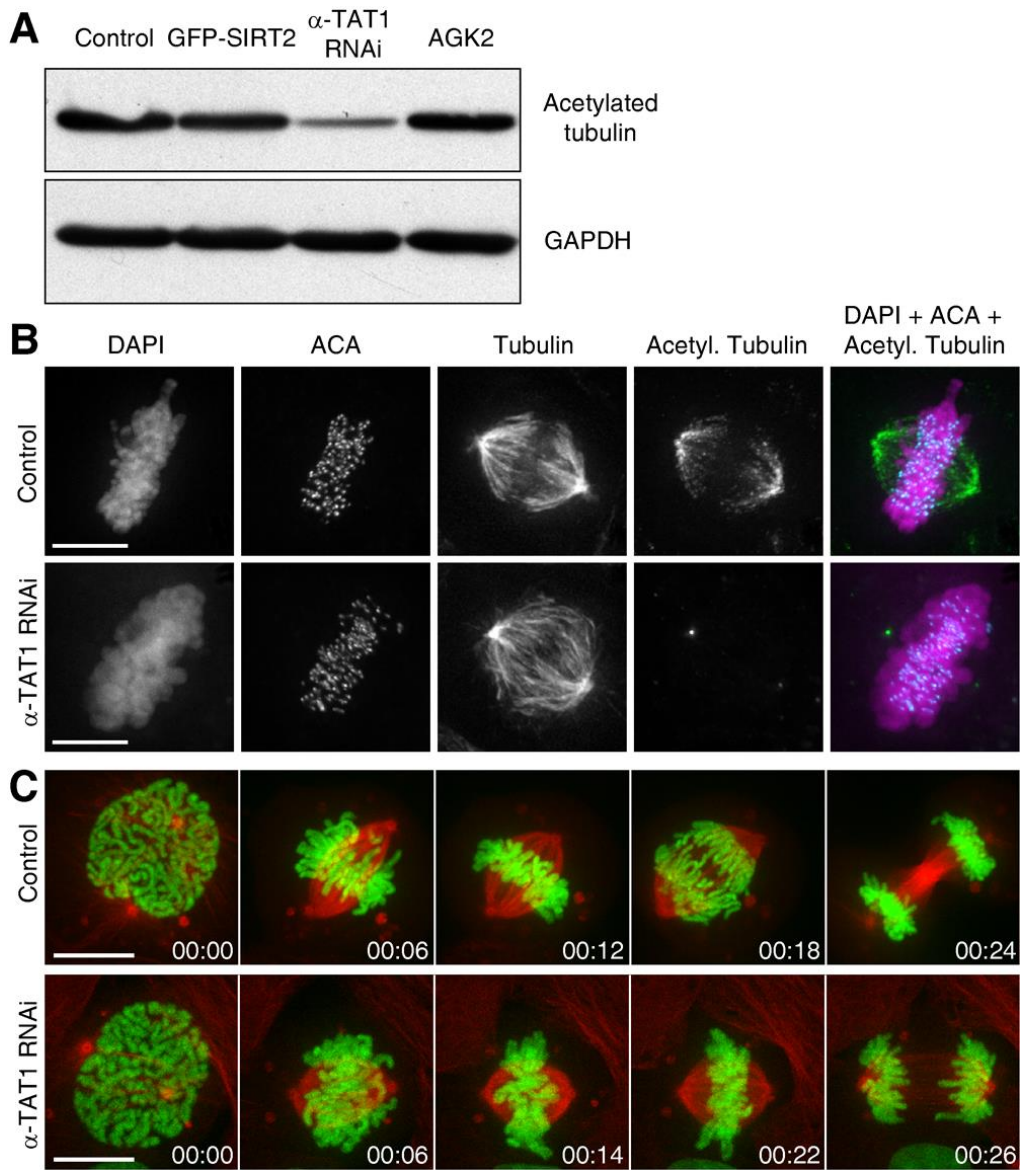


Fig. S5 – Chromosome congression does not depend on acetylation of spindle microtubules. (A) Immuno blotting for acetylated tubulin shows that RNAi knockdown of α -Tat1, a specific tubulin acetyl transferase (30, 41), reduced tubulin acetylation. However, overexpressed or inhibited Sirt2, a tubulin deacetylase (42), had no effect on tubulin acetylation, likely due to the action of other known tubulin deacetylases (43). Protein lysates of U2OS cells were obtained 24h after GFP-SIRT2 transfection, 48 h after α -TAT1 siRNA transfection (50 nM) and 4h after adding the SIRT2 inhibitor AGK2 (30 μ M). GAPDH was used as loading control. (B) Deconvolved wide-field immunofluorescence images of methanol-fixed U2OS cells stained for DNA (DAPI), kinetochores (ACA), α -tubulin and acetylated tubulin. Scale bar 10 μ m. (C) Spinning disk confocal live cell imaging of U2OS cells stably expressing H2B-GFP and mCherry- α -tubulin. Microtubule acetylation was prevented by α -TAT1 siRNA transfection (50 nM) and cells were recorded after 48h. Cells completed mitosis in 41 \pm 12 min (mean \pm SD). N = 9 cells from 2 independent experiments. Scale bar=10 μ m. Time = h:min.

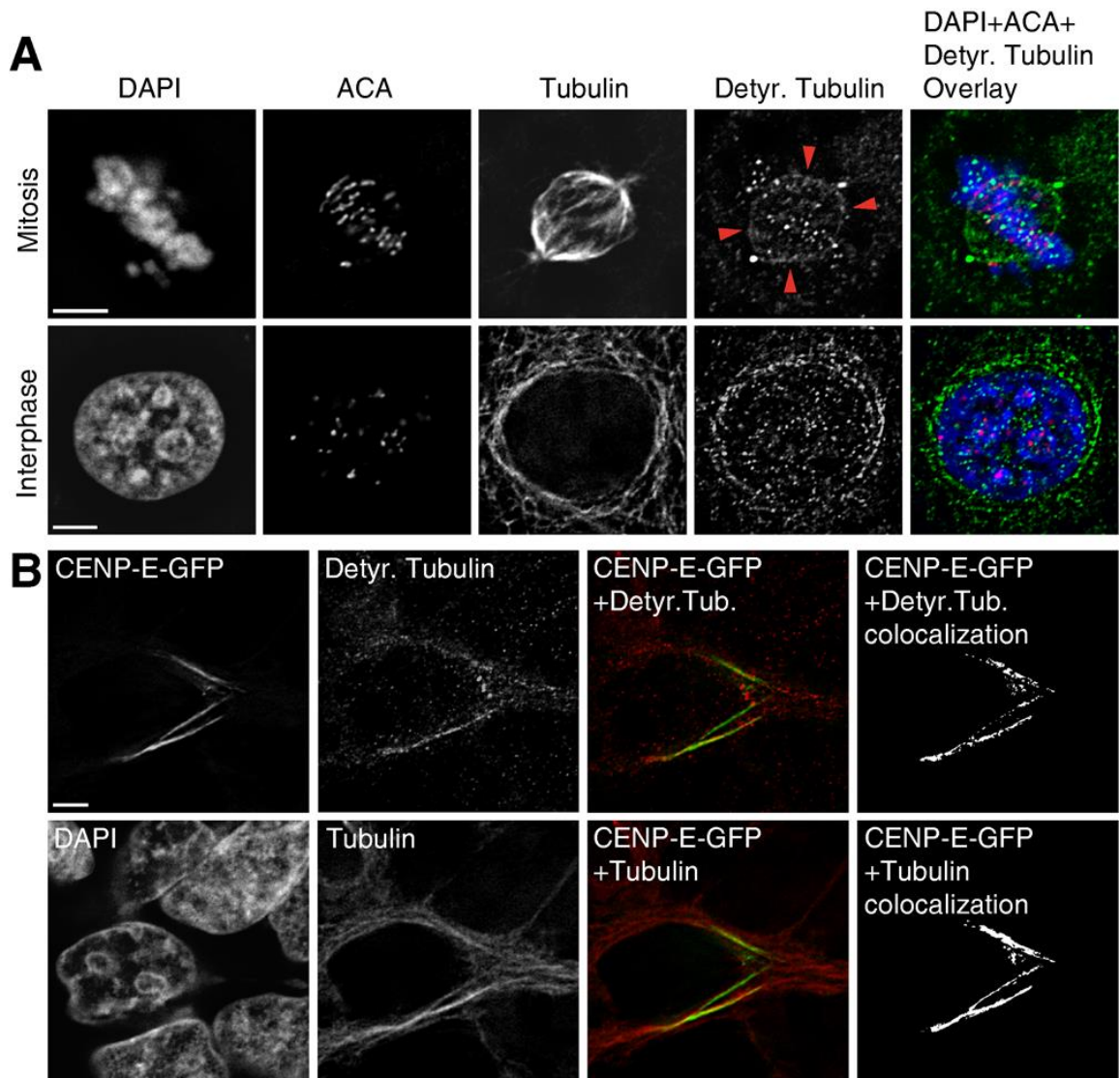


Fig. S6 – CENP-E colocalizes with detyrosinated microtubules during G2 in HeLa cells. (A) Deconvolved wide-field immunofluorescence images of methanol-fixed HeLa cells stained for DNA (DAPI), kinetochores (ACA), α -tubulin and detyrosinated tubulin. Red arrowheads highlight detyrosinated kinetochore microtubules in control cells. Scale bar=10 μ m. (B) Deconvolved wide-field immunofluorescence images of methanol-fixed HeLa cells stably expressing CENP-E-GFP stained for DNA (DAPI), α -tubulin and detyrosinated tubulin. CENP-E-GFP signal was detected by direct fluorescence. Colocalization analysis was performed in ImageJ. Scale bar=10 μ m.

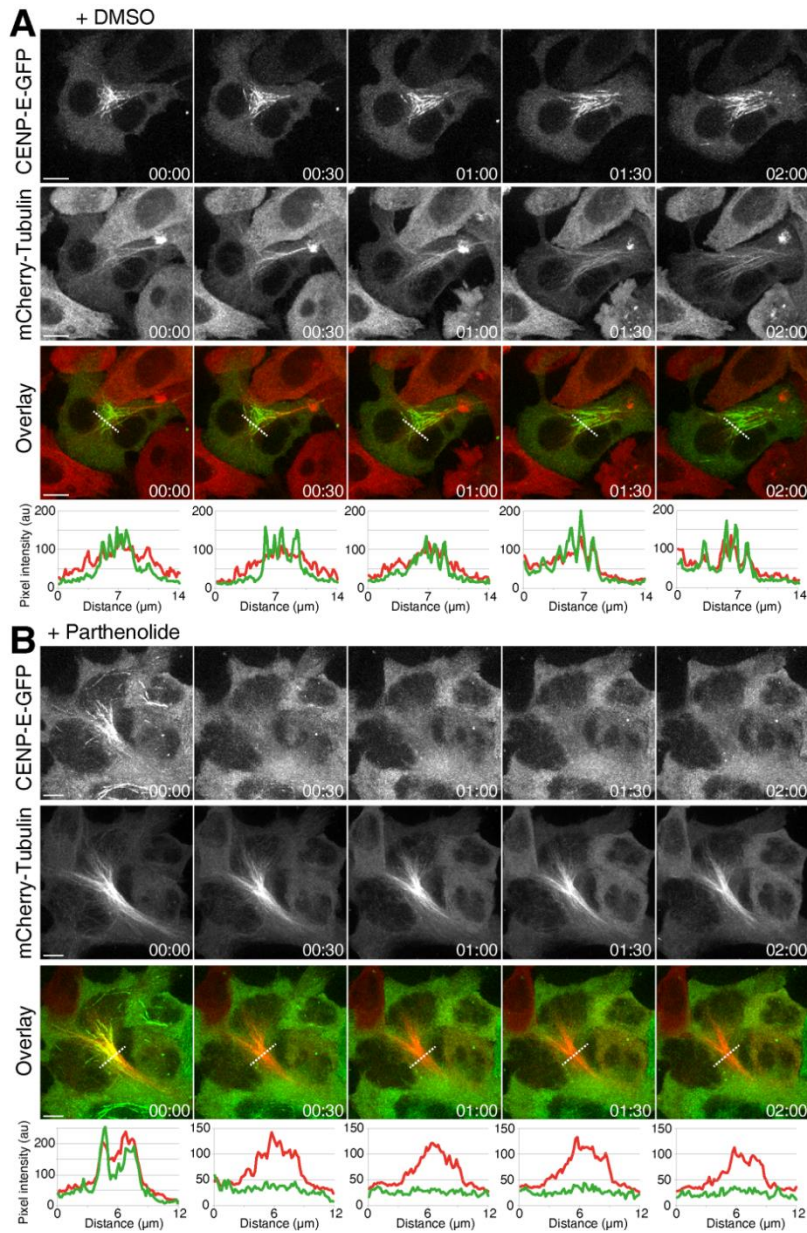


Fig. S7 – Inhibition of tubulin detyrosination dissociates CENP-E from microtubules in G2 cells. (A) HeLa cells stably expressing CENP-E-GFP were transiently transfected with mCherry-tubulin and recorded by spinning-disk confocal microscopy. 3h after addition of DMSO, CENP-E was still associated with microtubules of all control cells in G2 (58 cells, 2 independent experiments). Dashed lines represent the positions of line-scans used to quantify the fluorescence intensities of CENP-E (green) and tubulin (red), which are shown in corresponding diagrams. Scale bar=10 μm . Time = h:min. (B) CENP-E dissociates from microtubules 33 ± 16 min after addition of 20 μM parthenolide (90 cells, 3 independent experiments). Dashed lines represent the positions of line-scans used to quantify the fluorescence intensities of CENP-E (green) and tubulin (red), which are shown in corresponding diagrams. Scale bar=10 μm . Time = h:min.

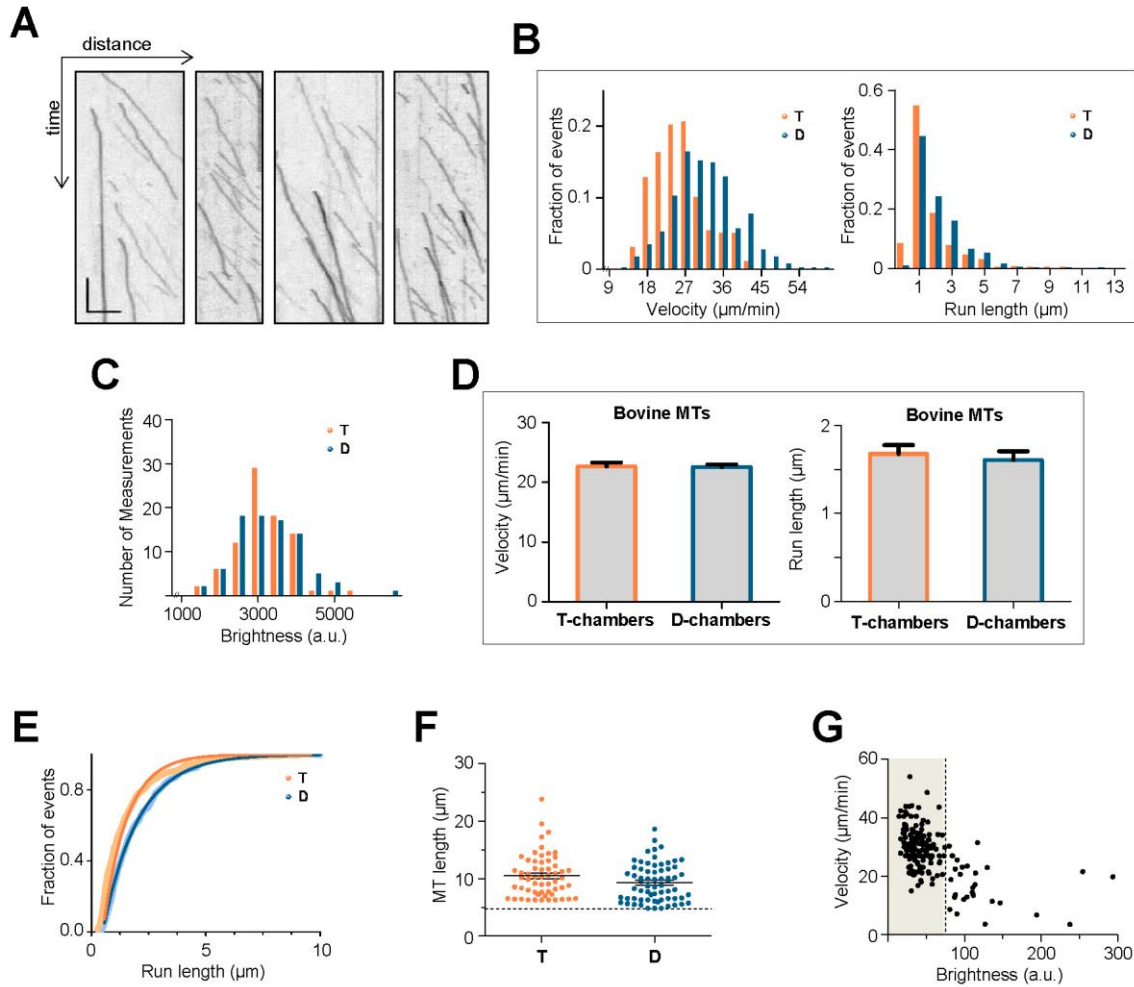


Fig. S8 - Quantitative analysis of CENP-E motility in vitro. (A) Example kymographs of single-molecule CENP-E motions on D-MTs. Scale bars: 8 s, 4 μm . (B) Histograms of velocity and run length of CENP-E on T-MTs vs. D-MTs; data from N=3 independent experiments for T-MTs, in which n=257 tracks were analyzed. For D-MTs N=4 and n=401. (C) Histograms of brightness of T- and D-MTs reveal similar incorporation of bovine HiLyte647 tubulin, which was used to assist microtubule visualization. Data based on N=3 independent experiments and n=84 analyzed microtubules of each type. (D) Velocity and run length of CENP-E-GFP on bovine microtubules that were added to the flow chambers also containing either T-MTs (T-chambers) or D-MTs (D-chambers). Same results were obtained on bovine microtubules in these different chambers: $p > 0.1$ with 95% confidence; n=121 and 171 in T- and D-chambers, respectively. (E) Cumulative distributions for run lengths. Lines are exponential fits (see Materials and Methods). (F) Length of microtubules used in motility experiments. Solid lines show Mean \pm SEM, horizontal broken line indicates that the minimal microtubule length for these analyses was 4.8 μm . (G) Velocity of CENP-E-GFP motions on D-MTs plotted vs. brightness of the moving dots suggests that larger complexes tend to walk slower. Highlighted area indicates the range for which the velocity did not correlate with brightness of the moving dots.

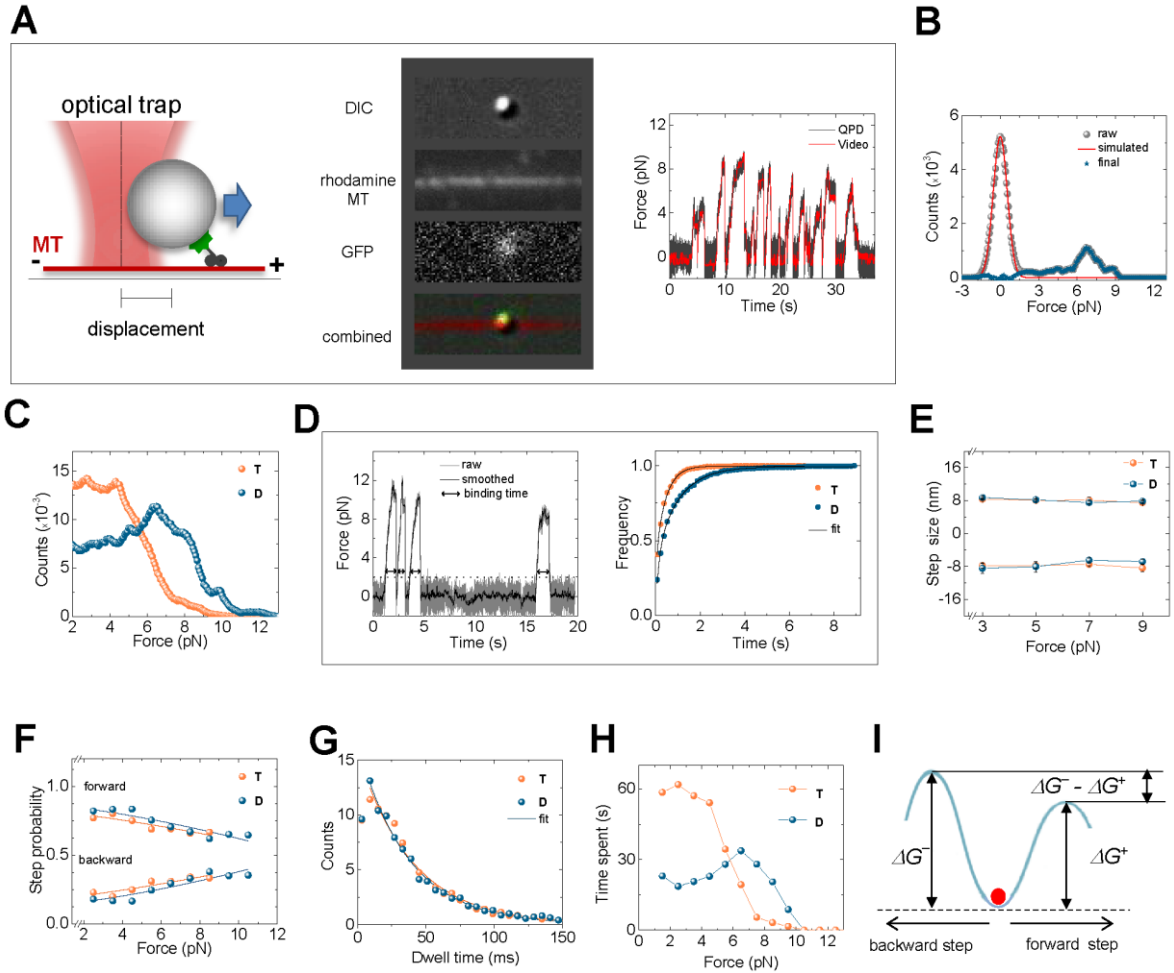


Fig. S9 - Analysis of CENP-E force generation. (A) Experimental diagram and images of a CENP-E-coated bead held in an optical trap: bead image in DIC, microtubule image in rhodamine channel and the GFP signal from CENP-E-GFP bead coating. Graph shows the QPD signal and video tracking data for sequence in Movie S4. The trap stiffness was 0.055 pN/nm. (B) A representative histogram distribution of force counts (gray) for one bead experiment (as in Fig 2C). Noise was subtracted as described in Materials and Methods. The resulting signals from all beads were summed to obtain distributions in Fig S9C. (C) All force spikes as in Fig 2C were processed to subtract noise, summed, normalized to the total number of counts and plotted for >2 pN. (D) Left panel illustrates the procedure for determining the duration of force spikes (binding time). The right panel shows cumulative distributions of the duration of force spikes with two-exponential fittings. For T- and D-MTs, the number of binding events was 604 and 394, respectively. (E) The step size of CENP-E in forward (positive) or backward (negative) direction does not change with increasing load. (F) Forward and backward stepping probability of CENP-E with theoretical fitting (solid lines; see Materials and Methods). (G) Distribution of dwell times for motor stepping for 1-10 pN range with a single exponential fit (solid curve). Total number of dwells was 6877 and 4541 for T- and D-MTs, respectively. (H) The distribution of total times spent by CENP-E beads within 1 pN force bins. (I) Illustration of the activation energy barriers for a motor (red dot) that steps forward and backward (see Materials and Methods for details).

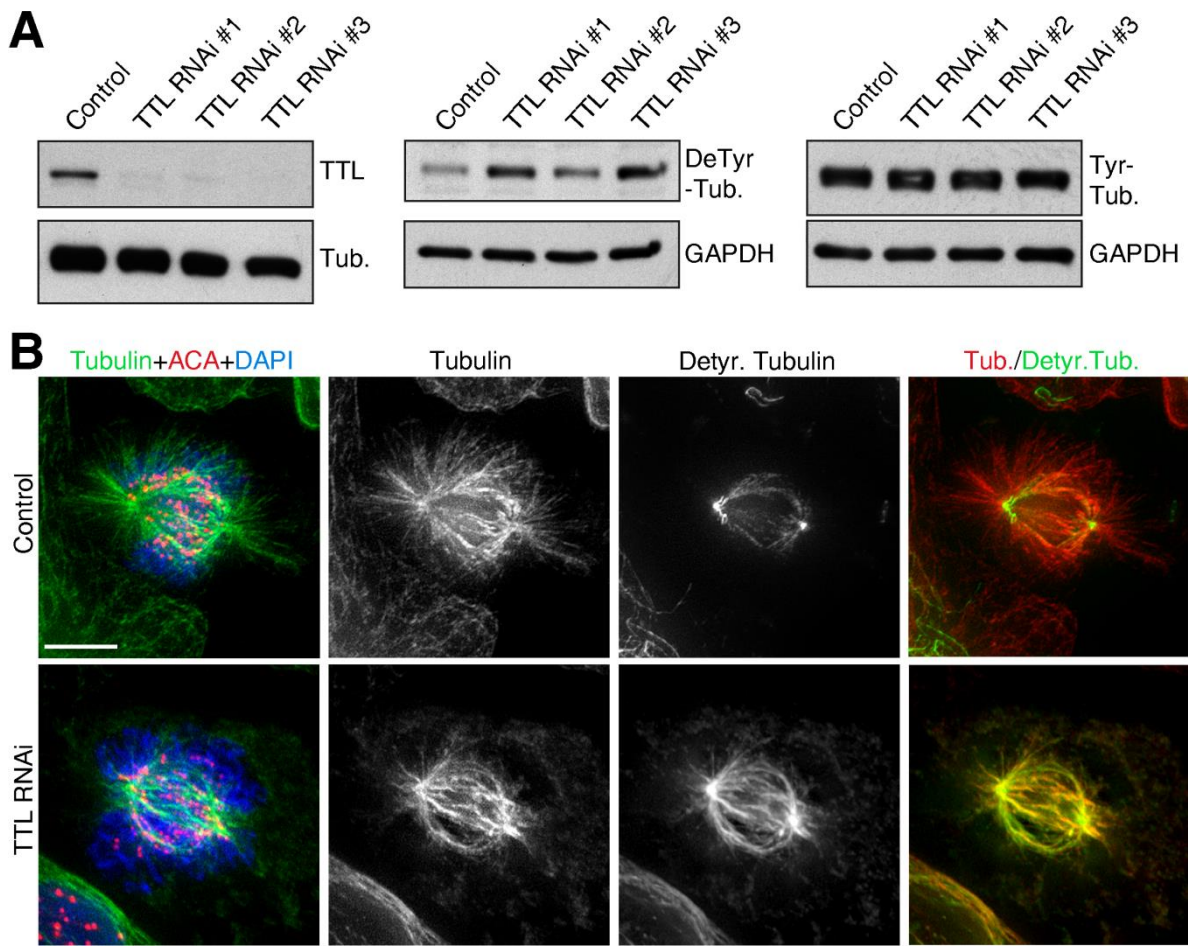


Fig. S10 – TTL depletion causes ubiquitous spindle microtubule detyrosination. (A) TTL was depleted in U2OS cells using three independent siRNAs. Protein lysates of U2OS cells were obtained 48h after transfection with TTL siRNAs, and the efficiency of RNAi-mediated TTL knockdown and microtubule tyrosination/detyrosination was examined by immunoblotting. GAPDH and tubulin were used as loading controls. (B) Deconvolved wide-field immunofluorescence images of methanol-fixed U2OS cells showing the redistribution of detyrosinated tubulin after TTL RNAi. Note the ubiquitous detyrosination of spindle microtubules, including astral microtubules. Scale bar = 5 μ m.

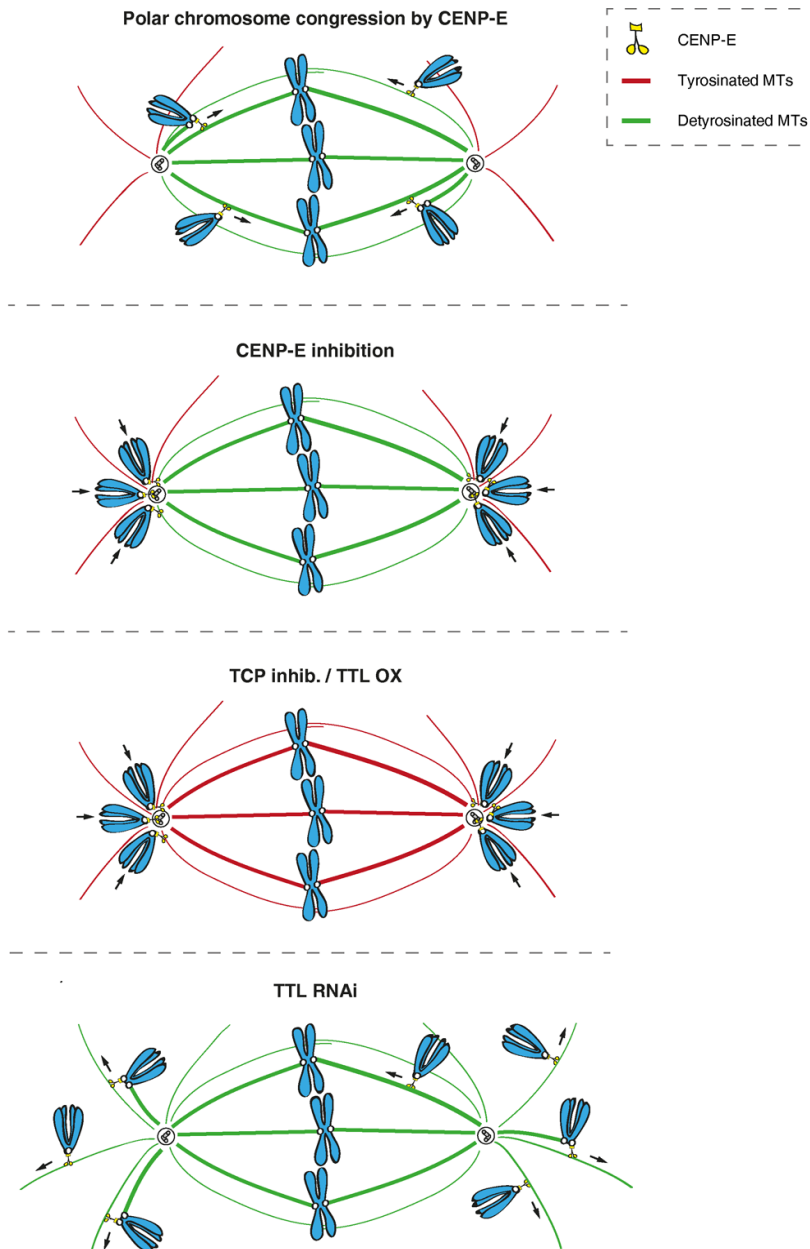


Fig. S11 – Model for the role of microtubule detyrosination in kinetochore-based chromosome motility during congression. Congression of pole-proximal chromosomes towards the metaphase plate relies on the kinetochore plus-end directed motor CENP-E (upper panel). Red color depicts tyrosinated microtubules, while green color depicts detyrosinated microtubules in the spindle. Arrows indicate directions of chromosome movements. Pole-proximal chromosomes do not congress and remain stuck at the poles when either CENP-E activity is abrogated or microtubule detyrosination is prevented by inhibiting TCP or overexpressing TTL (two middle panels). In contrast, TTL depletion causes the transport of pole-proximal chromosomes in random directions (bottom panel). This correlates with an overall increase in microtubule detyrosination in the spindle, disrupting the navigation system that normally guides CENP-E towards the spindle equator.

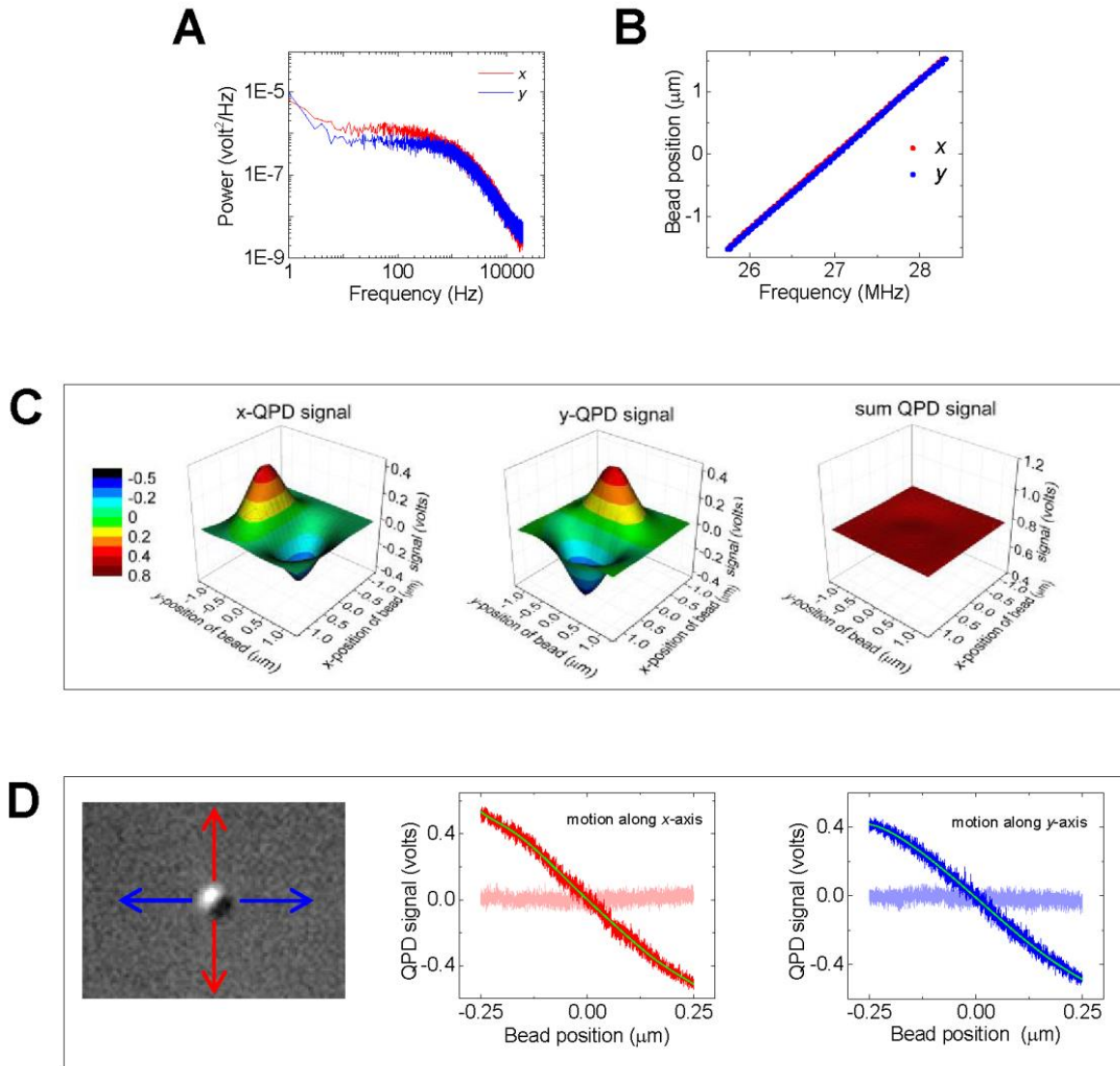


Fig. S12 – Optical trap calibration. (A) Lorentzian power spectrum of a $0.54\ \mu\text{m}$ polystyrene bead trapped with a laser beam (collected at $50\ \text{KHz}$ for $1\ \text{s}$) indicates a low level of mechanical noise. (B) Calibration plot to convert AOD input frequency into the bead displacement in x and y . Slope is $1.19\ \mu\text{m}/\text{MHz}$. (C) The graphs show QPD signals (x , y and sum) for different bead positions in the x,y plane and $z=0\ \mu\text{m}$. Coverslip-immobilized bead (diameter $0.54\ \mu\text{m}$) was moved from $-1.2\ \mu\text{m}$ to $1.2\ \mu\text{m}$ in x,y with $0.15\ \mu\text{m}$ steps using a piezo-electric stage. (D) DIC image of the bead and the directions of bead motions during the QPD calibration procedure. Trapped bead was moved with AOD from $-0.25\ \mu\text{m}$ to $0.25\ \mu\text{m}$ with $16\ \text{nm}$ steps along x - (red), and y - (blue) axes of the microscope. Corresponding QPD responses along the same axes are shown in dark color; signals in the direction perpendicular to bead motion are shown with light colors. Fitting (green) provides the conversion parameters from QPD voltage to bead displacement.

	energy difference at zero load $\Delta G^- - \Delta G^+$, $k_B T$	characteristic distance d , nm
CENP-E on T-MTs	1.56 ± 0.12	0.25 ± 0.04
CENP-E on D-MTs	2.05 ± 0.13	0.29 ± 0.05
Kinesin 1	5.90 ± 0.04	3.21 ± 0.72

Table S1 – Energy landscape for CENP-E stepping (Fig. S9I). The energy difference between the backward and forward activation barriers at zero load was calculated with equations (3) based on data in Fig. S9F. Characteristic distance against the load was calculated with equations (4) based on data in Fig. 2F. Data for kinesin 1 are from refs. (25, 26). This comparison shows that CENP-E motor tends to step backward at zero force more frequently than Kinesin 1, but CENP-E stepping is not nearly as sensitive to load.

Movie legends

Movie S1 – Congression of pole-proximal chromosomes is impaired after CENP-E inhibition, TTL overexpression or TCP inhibition. Spinning-disk confocal time-lapse imaging of U2OS cells stably expressing H2B-GFP and mCherry- α -tubulin under the indicated experimental conditions. Cells were recorded every 2 min. Time=h:min.

Movie S2 - Inhibition of tubulin carboxipeptidase with parthenolide dissociates CENP-E from microtubules in G2 cells. Spinning-disk confocal time-lapse imaging of HeLa cells stably expressing CENP-E-GFP and transfected with mCherry- α -tubulin under the indicated experimental conditions. Cells were recorded every 2 min. Time=h:min.

Movie S3 - CENP-E motility on tyrosinated and detyrosinated microtubules in vitro. Single molecules of CENP-E-GFP (green) walk on taxol-stabilized microtubules that were polymerized from tyrosinated (“Tyr MT”, red) or detyrosinated (“Det MT”, purple) human tubulin. Video is played at 30 fps, which is 3 times faster than recorded.

Movie S4 - Force generation by CENP-E motor. First image is an overlay of the DIC image of 0.54 μ m bead (grayscale), microtubule (red) and CENP-E-GFP (green); “+” symbol indicates microtubule polarity. All subsequent frames show motions of the bead (DIC) in a stationary laser trap. Images were acquired continuously every 10 ms, but the video shows only every 5th frame. Video is played at 30 fps, so the motions appear 1.4 times slower than recorded.

Movie S5 - Chromosomes cannot complete congression in TTL depleted cells and are randomly transported away from the spindle poles by CENP-E. Spinning-disk confocal time-lapse imaging of U2OS cells stably expressing GFP-CENP-A and mCherry- α -tubulin under the indicated experimental conditions. Cells were recorded every 2 min. Time=h:min.

References and Notes

1. M. Barisic, P. Aguiar, S. Geley, H. Maiato, Kinetochore motors drive congression of peripheral polar chromosomes by overcoming random arm-ejection forces. *Nat. Cell Biol.* **16**, 1249–1256 (2014). [Medline doi:10.1038/ncb3060](#)
2. T. M. Kapoor, M. A. Lampson, P. Hergert, L. Cameron, D. Cimini, E. D. Salmon, B. F. McEwen, A. Khodjakov, Chromosomes can congress to the metaphase plate before biorientation. *Science* **311**, 388–391 (2006). [Medline doi:10.1126/science.1122142](#)
3. C. E. Walczak, S. Cai, A. Khodjakov, Mechanisms of chromosome behaviour during mitosis. *Nat. Rev. Mol. Cell Biol.* **11**, 91–102 (2010). [Medline](#)
4. P. Kalab, R. Heald, The RanGTP gradient—A GPS for the mitotic spindle. *J. Cell Sci.* **121**, 1577–1586 (2008). [Medline doi:10.1242/jcs.005959](#)
5. T. Kiyomitsu, I. M. Cheeseman, Chromosome- and spindle-pole-derived signals generate an intrinsic code for spindle position and orientation. *Nat. Cell Biol.* **14**, 311–317 (2012). [Medline doi:10.1038/ncb2440](#)
6. Y. Kim, A. J. Holland, W. Lan, D. W. Cleveland, Aurora kinases and protein phosphatase 1 mediate chromosome congression through regulation of CENP-E. *Cell* **142**, 444–455 (2010). [Medline doi:10.1016/j.cell.2010.06.039](#)
7. J. Whyte, J. R. Bader, S. B. Tauhata, M. Raycroft, J. Hornick, K. K. Pfister, W. S. Lane, G. K. Chan, E. H. Hinchcliffe, P. S. Vaughan, K. T. Vaughan, Phosphorylation regulates targeting of cytoplasmic dynein to kinetochores during mitosis. *J. Cell Biol.* **183**, 819–834 (2008). [Medline doi:10.1083/jcb.200804114](#)
8. S. Cai, C. B. O’Connell, A. Khodjakov, C. E. Walczak, Chromosome congression in the absence of kinetochore fibres. *Nat. Cell Biol.* **11**, 832–838 (2009). [Medline doi:10.1038/ncb1890](#)
9. K. J. Verhey, J. Gaertig, The tubulin code. *Cell Cycle* **6**, 2152–2160 (2007). [Medline doi:10.4161/cc.6.17.4633](#)
10. C. Janke, The tubulin code: Molecular components, readout mechanisms, and functions. *J. Cell Biol.* **206**, 461–472 (2014). [Medline](#)
11. G. G. Gundersen, J. C. Bulinski, Distribution of tyrosinated and nontyrosinated alpha-tubulin during mitosis. *J. Cell Biol.* **102**, 1118–1126 (1986). [Medline doi:10.1083/jcb.102.3.1118](#)
12. P. J. Wilson, A. Forer, Acetylated α -tubulin in spermatogenic cells of the crane fly *Nephrotoma suturalis*: Kinetochore microtubules are selectively acetylated. *Cell Motil. Cytoskeleton* **14**, 237–250 (1989). [doi:10.1002/cm.970140210](#)
13. G. G. Gundersen, M. H. Kalnoski, J. C. Bulinski, Distinct populations of microtubules: Tyrosinated and nontyrosinated α tubulin are distributed differently in vivo. *Cell* **38**, 779–789 (1984). [Medline doi:10.1016/0092-8674\(84\)90273-3](#)
14. N. A. Reed, D. Cai, T. L. Blasius, G. T. Jih, E. Meyhofer, J. Gaertig, K. J. Verhey, Microtubule acetylation promotes kinesin-1 binding and transport. *Curr. Biol.* **16**, 2166–2172 (2006). [Medline doi:10.1016/j.cub.2006.09.014](#)

15. Y. Konishi, M. Setou, Tubulin tyrosination navigates the kinesin-1 motor domain to axons. *Nat. Neurosci.* **12**, 559–567 (2009). [Medline doi:10.1038/nn.2314](#)
16. J. W. Hammond, C. F. Huang, S. Kaech, C. Jacobson, G. Banker, K. J. Verhey, Posttranslational modifications of tubulin and the polarized transport of kinesin-1 in neurons. *Mol. Biol. Cell* **21**, 572–583 (2010). [Medline doi:10.1091/mbc.E09-01-0044](#)
17. M. Sirajuddin, L. M. Rice, R. D. Vale, Regulation of microtubule motors by tubulin isotypes and post-translational modifications. *Nat. Cell Biol.* **16**, 335–344 (2014). [Medline doi:10.1038/ncb2920](#)
18. K. Ersfeld, J. Wehland, U. Plessmann, H. Dodemont, V. Gerke, K. Weber, Characterization of the tubulin-tyrosine ligase. *J. Cell Biol.* **120**, 725–732 (1993). [Medline doi:10.1083/jcb.120.3.725](#)
19. X. Fonrose, F. Ausseil, E. Soleilhac, V. Masson, B. David, I. Pouny, J. C. Cintrat, B. Rousseau, C. Barette, G. Massiot, L. Lafanechère, Parthenolide inhibits tubulin carboxypeptidase activity. *Cancer Res.* **67**, 3371–3378 (2007). [Medline doi:10.1158/0008-5472.CAN-06-3732](#)
20. I. Poser, M. Sarov, J. R. Hutchins, J. K. Hériché, Y. Toyoda, A. Pozniakovsky, D. Weigl, A. Nitzsche, B. Hegemann, A. W. Bird, L. Pelletier, R. Kittler, S. Hua, R. Naumann, M. Augsburg, M. M. Sykora, H. Hofemeister, Y. Zhang, K. Nasmyth, K. P. White, S. Dietzel, K. Mechtler, R. Durbin, A. F. Stewart, J. M. Peters, F. Buchholz, A. A. Hyman, BAC TransgeneOmics: A high-throughput method for exploration of protein function in mammals. *Nat. Methods* **5**, 409–415 (2008). [Medline doi:10.1038/nmeth.1199](#)
21. T. J. Yen, G. Li, B. T. Schaar, I. Szilak, D. W. Cleveland, CENP-E is a putative kinetochore motor that accumulates just before mitosis. *Nature* **359**, 536–539 (1992). [Medline doi:10.1038/359536a0](#)
22. Materials and methods are available as supplementary materials on *Science Online*.
23. N. Gudimchuk, B. Vitre, Y. Kim, A. Kiyatkin, D. W. Cleveland, F. I. Ataullakhanov, E. L. Grishchuk, Kinetochore kinesin CENP-E is a processive bi-directional tracker of dynamic microtubule tips. *Nat. Cell Biol.* **15**, 1079–1088 (2013). [Medline doi:10.1038/ncb2831](#)
24. H. Yardimci, M. van Duffelen, Y. Mao, S. S. Rosenfeld, P. R. Selvin, The mitotic kinesin CENP-E is a processive transport motor. *Proc. Natl. Acad. Sci. U.S.A.* **105**, 6016–6021 (2008). [Medline doi:10.1073/pnas.0711314105](#)
25. N. J. Carter, R. A. Cross, Mechanics of the kinesin step. *Nature* **435**, 308–312 (2005). [Medline doi:10.1038/nature03528](#)
26. M. Nishiyama, H. Higuchi, T. Yanagida, Chemomechanical coupling of the forward and backward steps of single kinesin molecules. *Nat. Cell Biol.* **4**, 790–797 (2002). [Medline doi:10.1038/ncb857](#)
27. L. Peris, M. Thery, J. Fauré, Y. Saoudi, L. Lafanechère, J. K. Chilton, P. Gordon-Weeks, N. Galjart, M. Bornens, L. Wordeman, J. Wehland, A. Andrieux, D. Job, Tubulin tyrosination is a major factor affecting the recruitment of CAP-Gly proteins at

- microtubule plus ends. *J. Cell Biol.* **174**, 839–849 (2006). [Medline](#)
[doi:10.1083/jcb.200512058](#)
28. M. Barisic, B. Sohm, P. Mikolcevic, C. Wandke, V. Rauch, T. Ringer, M. Hess, G. Bonn, S. Geley, Spindly/CCDC99 is required for efficient chromosome congression and mitotic checkpoint regulation. *Mol. Biol. Cell* **21**, 1968–1981 (2010). [Medline](#)
[doi:10.1091/mbc.E09-04-0356](#)
29. A. E. Prota, M. M. Magiera, M. Kuijpers, K. Bargsten, D. Frey, M. Wieser, R. Jaussi, C. C. Hoogenraad, R. A. Kammerer, C. Janke, M. O. Steinmetz, Structural basis of tubulin tyrosination by tubulin tyrosine ligase. *J. Cell Biol.* **200**, 259–270 (2013). [Medline](#)
[doi:10.1083/jcb.201211017](#)
30. T. Shida, J. G. Cueva, Z. Xu, M. B. Goodman, M. V. Nachury, The major α -tubulin K40 acetyltransferase alphaTAT1 promotes rapid ciliogenesis and efficient mechanosensation. *Proc. Natl. Acad. Sci. U.S.A.* **107**, 21517–21522 (2010). [Medline](#)
[doi:10.1073/pnas.1013728107](#)
31. C. A. Schneider, W. S. Rasband, K. W. Eliceiri, NIH Image to ImageJ: 25 years of image analysis. *Nat. Methods* **9**, 671–675 (2012). [Medline](#) [doi:10.1038/nmeth.2089](#)
32. A. Hyman, D. Drechsel, D. Kellogg, S. Salser, K. Sawin, P. Steffen, L. Wordeman, T. Mitchison, Preparation of modified tubulins. *Methods Enzymol.* **196**, 478–485 (1991).
[Medline](#) [doi:10.1016/0076-6879\(91\)96041-O](#)
33. Y. Kim, J. E. Heuser, C. M. Waterman, D. W. Cleveland, CENP-E combines a slow, processive motor and a flexible coiled coil to produce an essential motile kinetochore tether. *J. Cell Biol.* **181**, 411–419 (2008). [Medline](#) [doi:10.1083/jcb.200802189](#)
34. V. A. Volkov, A. V. Zaytsev, E. L. Grishchuk, Preparation of segmented microtubules to study motions driven by the disassembling microtubule ends. *J. Vis. Exp.* 10.3791/51150 (2014). [Medline](#)
35. K. S. Thorn, J. A. Ubersax, R. D. Vale, Engineering the processive run length of the kinesin motor. *J. Cell Biol.* **151**, 1093–1100 (2000). [Medline](#) [doi:10.1083/jcb.151.5.1093](#)
36. E. L. Grishchuk, A. K. Efremov, V. A. Volkov, I. S. Spiridonov, N. Gudimchuk, S. Westermann, D. Drubin, G. Barnes, J. R. McIntosh, F. I. Ataullakhanov, The Dam1 ring binds microtubules strongly enough to be a processive as well as energy-efficient coupler for chromosome motion. *Proc. Natl. Acad. Sci. U.S.A.* **105**, 15423–15428 (2008).
[Medline](#) [doi:10.1073/pnas.0807859105](#)
37. M. P. Sheetz, Ed, *Laser Tweezers in Cell Biology* (Academic Press, San Diego, 1998).
38. J. W. J. Kerssemakers, E. L. Munteanu, L. Laan, T. L. Noetzel, M. E. Janson, M. Dogterom, Assembly dynamics of microtubules at molecular resolution. *Nature* **442**, 709–712 (2006). [Medline](#) [doi:10.1038/nature04928](#)
39. M. Nishiyama, H. Higuchi, T. Yanagida, Chemomechanical coupling of the forward and backward steps of single kinesin molecules. *Nat. Cell Biol.* **4**, 790–797 (2002). [Medline](#)
[doi:10.1038/ncb857](#)
40. J. Howard, *Mechanics of Motor Proteins and the Cytoskeleton* (Sinauer Associates, Sunderland, MA, 2001), chap. 15.

41. J. S. Akella, D. Wloga, J. Kim, N. G. Starostina, S. Lyons-Abbott, N. S. Morrissette, S. T. Dougan, E. T. Kipreos, J. Gaertig, MEC-17 is an α -tubulin acetyltransferase. *Nature* **467**, 218–222 (2010). [Medline doi:10.1038/nature09324](#)
42. B. J. North, B. L. Marshall, M. T. Borra, J. M. Denu, E. Verdin, The human Sir2 ortholog, SIRT2, is an NAD⁺-dependent tubulin deacetylase. *Mol. Cell* **11**, 437–444 (2003). [Medline doi:10.1016/S1097-2765\(03\)00038-8](#)
43. C. Hubbert, A. Guardiola, R. Shao, Y. Kawaguchi, A. Ito, A. Nixon, M. Yoshida, X. F. Wang, T. P. Yao, HDAC6 is a microtubule-associated deacetylase. *Nature* **417**, 455–458 (2002). [Medline doi:10.1038/417455a](#)